

Hyperspectral and thermal temperature estimation during laser cladding

Cite as: J. Laser Appl. **31**, 022313 (2019); <https://doi.org/10.2351/1.5096129>

Submitted: 14 March 2019 • Accepted: 14 March 2019 • Published Online: 22 April 2019

Margot Lison, Wim Devesse, Dieter de Baere, et al.

COLLECTIONS

Paper published as part of the special topic on [Proceedings of the International Congress of Applications of Lasers & Electro-Optics \(ICALEO® 2018\)](#)



View Online



Export Citation



CrossMark

ARTICLES YOU MAY BE INTERESTED IN

[Spectroscopic monitoring and melt pool temperature estimation during the laser metal deposition process](#)

Journal of Laser Applications **28**, 022303 (2016); <https://doi.org/10.2351/1.4943995>

[Hardware-in-the-loop control of additive manufacturing processes using temperature feedback](#)

Journal of Laser Applications **28**, 022302 (2016); <https://doi.org/10.2351/1.4943911>

[Powder catchment in laser metal deposition](#)

Journal of Laser Applications **31**, 022308 (2019); <https://doi.org/10.2351/1.5096130>



The professional society for
lasers, laser applications,
and laser safety worldwide.

Become part of the LIA experience -
cultivating innovation, ingenuity, and
inspiration within the laser community.

Find Out More



www.lia.org/membership
membership@lia.org

Hyperspectral and thermal temperature estimation during laser cladding

Cite as: J. Laser Appl. 31, 022313 (2019); doi: 10.2351/1.5096129

Submitted: 14 March 2019 · Accepted: 14 March 2019 ·

Published Online: 22 April 2019



Margot Lison, Wim Devesse, Dieter de Baere, Michaël Hinderdael, and Patrick Guillaume

AFFILIATIONS

Acoustics and Vibration Research Group, Vrije Universiteit Brussel, Pleinlaan 2, B-1050 Brussels, Belgium

Note: This paper is part of the Special Collection: Proceedings of the International Congress of Applications of Lasers & Electro-Optics (ICALEO® 2018).

ABSTRACT

Although there is no doubt about the tremendous industrial potential of metal additive manufacturing techniques such as laser metal deposition, the technology still has some intrinsic quality challenges to overcome before reaching its industrial maturity. Noncontact *in situ* monitoring of the temperature evolution of the workpiece could provide the necessary information to implement an automated closed-loop process control system and optimize the manufacturing process, providing a robust solution to these issues. However, measuring absolute temperatures is not self-evident: wavelength-dependent emissivity values vary between solid, liquid, and mushy metallic regions, requiring spectral information and dedicated postprocessing to relate the amount of emitted infrared radiation to the material temperature. This paper compares the temperature estimation results obtained from a visible and near-infrared hyperspectral line camera and a conventional short-wave infrared (SWIR) thermal camera during the laser melting and cladding of a 316L steel sample. Both methods show agreeing results for the temperature distribution inside the melt pool, with the SWIR camera extending the temperature measurements beyond the melt pool boundaries into the solid region.

Key words: laser cladding, additive manufacturing, temperature estimation, thermal monitoring, hyperspectral imaging

© 2019 Laser Institute of America. <https://doi.org/10.2351/1.5096129>

I. INTRODUCTION

In terms of design flexibility and efficient use of materials, there are no manufacturing techniques that create as many opportunities as additive manufacturing. Although promising, the technology has not yet reached the point where it is robust enough to produce metallic components for high-end applications in, among others, aerospace and automotive industries. The technology is currently typically implemented in an open-loop configuration, due to a limited understanding of the link between production parameters and the complex physical phenomena that influence the finished product's structural quality.¹

The use of a highly focused laser beam that melts and fuses metallic material into a near-net-shaped product creates very local temperature elevations and high thermal gradients, which strongly influence the material properties and geometrical accuracy of the manufactured component. Monitoring the temperature behavior of the melt pool and the created clad is an efficient means to derive information regarding the printed part's overall quality and has the

potential to lay the foundation for automated closed-loop control strategies which can increase the technology's repeatability and reliability significantly. It is therefore the subject of a lot of ongoing research,^{2,3} one of the remaining challenges being the accurate estimation of the true temperature values observed in the liquid melt pool, the solid clad, and the mushy transition zone. Conventional contactless monitoring methods involve multiwavelength pyrometers and infrared thermographic cameras.⁴ In both cases, the temperature estimations are based on rather blunt assumptions regarding the material's emissivity properties in order to convert the incoming radiation intensity to an absolute temperature value. While treating the object as a gray body is often the only viable option using these devices, it can lead to significant errors. Among others, the emissivity of an object is often an unknown function of material composition, wavelength, surface morphology, phase, and temperature,⁵ reducing the temperature estimation to a mathematical problem which cannot be solved directly.

A recent development in overcoming this challenge is the use of a hyperspectral line camera to collect infrared radiation at

different wavelengths during laser cladding, which is then used to deduce an upper and lower limit of the melt pool temperature by subjecting the spectrum to a suitable curve fitting procedure which takes into account the wavelength dependency of the emissivity.⁶ This method improves upon the use of thermal cameras and pyrometers by collecting the spectral data of a larger amount of wavelengths compared to pyrometric methods, thereby increasing the signal-to-noise ratio, while retaining the high spatial resolution associated with camera-based systems.

While able to measure absolute temperature values in the liquid region of a melt pool with an uncertainty of about 10% during the laser cladding of 316L steel,⁷ the hyperspectral system, which operates in the visible and near-infrared (VNIR) spectrum, is not sufficiently sensitive to the radiation coming from the lower temperatures outside the melt pool to provide reliable temperature estimations for these solid regions.

The aim of this paper is to compare the melt pool temperatures calculated from the hyperspectral VNIR measurements to the thermograms recorded by a conventional thermal camera operating in the short-wave infrared (SWIR) spectrum. Its sensitivity to larger wavelengths makes the latter option more suitable for the measurement of low temperatures and may reveal information about the temperatures outside the melt pool which was previously unavailable to the hyperspectral VNIR measurement system.

Due to the lack of spectral information provided by the SWIR camera, the temperature estimations based on these measurements will be less sophisticated than is the case with the hyperspectral data. However, the SWIR camera has the advantage of creating two-dimensional thermal visualizations of the melt pool and its surroundings. These thermal images could offer an intuitive assessment of the temperature profiles derived from the hyperspectral line camera measurements.

Section II describes the experimental setup used to obtain the thermal information from a melt pool during the laser cladding and melting of 316L stainless steel, followed by an explanation of how these measurements are converted into absolute temperature values for each camera-based monitoring system. The resulting thermograms and temperature curves are then presented and discussed, followed by some concluding remarks.

II. EXPERIMENTAL SETUP

The experiments presented in this paper were performed by focusing a laser beam on a 316L stainless steel substrate, which undergoes a translational motion at a speed of 0.5 m/min (Fig. 1). A few moments into the process, this creates a steady-state melt pool whose size depends on the laser power. The laser, which is a flat top 1 kW fiber laser (IPG YLS-1000) with a diameter of 1.2 mm, has been used at two power settings: at 350 W during the so-called low laser power tests, and at 500 W for high laser power. At each laser power setting, an experiment was conducted inside an argon environment with and without the addition of a flow of metal powder particles, denoted as laser cladding and laser melting experiments, respectively. The coaxially added powder was of the type LPW 316L 44-106 μm and was fed to the melt pool at a mass flow rate of 2.1 g/min.

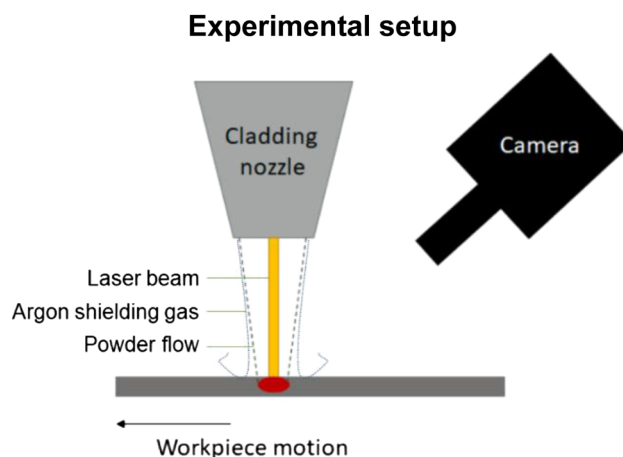


FIG. 1. Schematic overview of the experimental setup.

These four processes (laser melting and laser cladding at low and high laser power) have been monitored by two different camera-based thermal monitoring systems, which collected thermal measurements in and around the melt pool. The first is a SPECIM PFD V10E hyperspectral line camera, which measures the spectra in the VNIR region (400–950 nm) of a line of closely spaced points going laterally through the center of the melt pool with a spatial resolution of 12 $\mu\text{m}/\text{pixel}$ and a spectral resolution of 1.1 nm/pixel. The exposure time was set to 78 μs . The camera was calibrated using the spectrum measured from an Optronic Laboratories OL455 integrating sphere calibration source with a halogen lamp. The ratio between the measured spectrum and the spectrum registered by a NIST traceable JETI Specbos 1211 spectroradiometer provides the correction factor for the optical sensitivity of the hyperspectral camera. The second monitoring system comprises of a Xenics Xeva-1.7-320 InGaAs camera, which measures the collective radiant energy in the SWIR spectrum (900–1700 nm). Unlike a hyperspectral system, this camera does not measure specific spectral information, but it does provide a two-dimensional visualization of the melt pool and its surroundings with a spatial resolution of 40 $\mu\text{m}/\text{pixel}$. The exposure time of the camera was set to 10 μs during high power tests and 20 μs at low laser power.

The SWIR and hyperspectral VNIR cameras were inclined at an angle of, respectively, 34° and 38° relative to the normal surface while monitoring the melt pool on the stainless steel substrate. The measurements of both cameras were made at a frame rate of 1000 Hz and sent to a frame grabber via a CameraLink interface, before being processed on a personal computer according to the temperature estimation procedures described in Sec. III.

III. TEMPERATURE ESTIMATION

The thermal data collected by the two camera-based systems was used to make an estimation of the absolute temperature distribution inside the melt pool and its immediate surroundings.

Depending on the measurement system, two temperature estimation approaches are used.

A. SWIR thermal data

According to Planck's law,⁸ the spectral radiance B ($\text{W m}^{-3} \text{sr}^{-1}$) emitted by a black body is a function of the wavelength λ and temperature T according to

$$B(\lambda, T) = \frac{2hc^2}{\lambda^5} \frac{1}{\exp(hc/b\lambda T) - 1}. \quad (1)$$

Here, b is the Boltzmann constant, c is the speed of light, and h is the Planck constant. Real objects do not behave like black bodies, but follow similar behavior modified by a spectral emissivity parameter ε which lies between 0 and 1. The actual spectral radiance R emitted by the thermal body takes on the following form:

$$R(\lambda, T) = \varepsilon(\lambda) \cdot B(\lambda, T). \quad (2)$$

The measurements made with the thermal SWIR camera do not provide any individual spectral information, but instead provide an analog-to-digital unit (ADU) which is proportional to the collective radiation energy recorded by the sensor during a certain exposure time. Since the position of the camera remained fixed throughout the experiments, the registered radiant power (W) can be directly correlated to the spectrally integrated radiance over the SWIR range ($\text{W m}^2 \text{sr}^{-1}$). Assuming a gray body, i.e., a body whose emissivity does not depend on wavelength, and correcting the black body curves to take into account the photoresponsivity of the SWIR sensor, relative ADU values can be plotted against the corresponding measured temperatures. This approach implies assuming a linear analog-to-digital conversion in the camera and neglecting any effects of the lens on the

optic sensitivity of the measurement system. In order to rescale the curve to absolute 14-bit ADU values, the relative ADU values are multiplied by a constant so that the melting point of 316L stainless steel, which is around 1670 K,⁹ corresponds to the ADU value at which the observed material starts to melt when the laser is turned on. This was done separately for the two exposure times that were used during the experiments at low and high laser power, resulting in the temperature conversion curves displayed in Fig. 2.

This temperature estimation method deals with the unknown emissivity values by considering a constant emissivity over the complete field of view of the camera (liquid, mushy, and solid material) and by assuming the emissivity to be independent of the wavelength inside the SWIR region. Theory¹⁰ and experiments^{11,12} have shown that the spectral emissivity values of metals exhibit a decreasing linear dependency on wavelengths within the SWIR spectrum. The slopes for these large wavelengths are however relatively small, which makes the gray body approximation an appropriate assumption.

B. VNIR hyperspectral data

Assuming the spectral emissivity to be wavelength independent is however no longer valid in the VNIR range. It is more appropriate to describe the spectral emissivity as a linearly decreasing function of wavelength:

$$\varepsilon(\lambda) = B_\varepsilon - A_\varepsilon \frac{\lambda - \lambda_1}{\lambda_N - \lambda_1}. \quad (3)$$

In this equation, the constants A_ε and B_ε are constrained by $0 \leq A_\varepsilon \leq B_\varepsilon \leq 1$ in order to get a negative slope and an emissivity value which is smaller than or equal to 1. Unlike the thermal SWIR camera, the hyperspectral VNIR measurement system is able to provide the spectral radiance values for a range of different wavelengths. Fitting the measured spectrum to a black body model with a linearly decreasing spectral emissivity is a matter of solving the following least squares problem:

$$(\hat{A}_\varepsilon, \hat{B}_\varepsilon, T) = \arg \min \sum_{i=1}^N \frac{|R(\varepsilon_i, T_i) - \{B_\varepsilon - A_\varepsilon[(\lambda_i - \lambda_1)/(\lambda_N - \lambda_1)]\}B(\lambda_i, T)|^2}{\sigma_i^2}. \quad (4)$$

The cost function is weighted by the inverse of the variance of the measurements σ_i^2 , limiting the influence of noisy measurements on the temperature and emissivity calculations. A minimizing solution can be found for Eq. (4) by first setting the slope A_ε to zero, thus assuming a gray body, and next setting the offset B_ε to 1 while leaving the value of the slope free, fixing the offset and determining the optimal negative slope. This results in the upper and lower bounds of the actual melt pool temperature distribution, respectively.

IV. RESULTS AND DISCUSSION

Thermal measurements and temperature estimations were made for two types of laser-based experiments, namely, laser

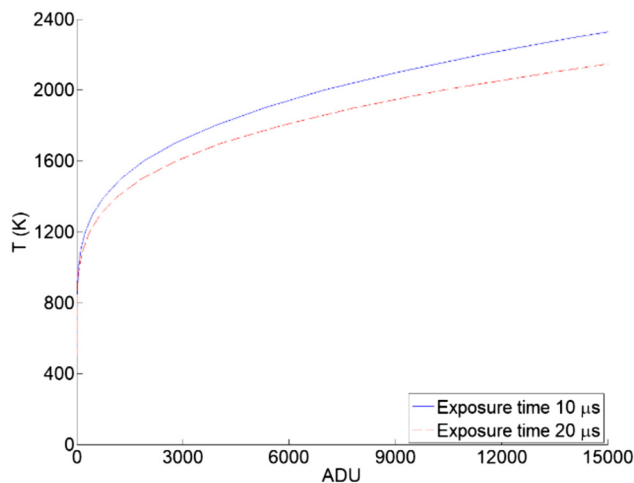


FIG. 2. Temperature conversion curves for SWIR measurements at two different exposure times.

melting and laser cladding. First, a discussion of the results obtained during laser melting will be presented, followed by the observations made during the more challenging laser cladding experiments.

A. Laser melting

Unlike laser cladding, no external material flow is added to the melt pool during laser melting. This results in the creation of a stable melt pool which shows little fluctuations in time. The SWIR and hyperspectral VNIR results presented in Sec. IV B are time averaged over 50 frames and 300 frames, respectively, which corresponds to 0.05 s and 0.3 s.

Figure 3 depicts the SWIR thermogram of the steady-state melt pool during a melting experiment at 350 W, which is characterized by a prominent mushy zone containing both solid and liquid material near the front and sides of the melt pool and a large fully liquid region in the center. Taking a line of pixels going laterally through the origin of the thermogram, the approximated temperature profile across the melt pool is displayed in Fig. 4. A horizontal dotted line indicates the melting point of 316L steel, but even without the knowledge of the melting line, the distinction between liquid, mushy, and solid regions can easily be made based on the shape of the temperature profile.

The temperature inside the liquid melt pool lowers gradually toward the melt pool edges, which are located around -520 and $520\ \mu\text{m}$, and then shows a decrease in its cooling gradient as it enters the mushy region until -600 and $640\ \mu\text{m}$. While this liquid–solid interface is only a few pixels wide in the SWIR thermogram, it is clearly indicated by the decline in cooling rate, which is a result of the phase changes taking place in the mushy region.

These observations are in good agreement with the advanced temperature estimations using the hyperspectral VNIR measurements, which are shown in Fig. 5. It should be noted that the apparent local temperature peak between -200 and $200\ \mu\text{m}$ in the SWIR measurements is the likely result of the returning melt pool reflection on the cladding nozzle, which appears as a white ring on the thermogram in Fig. 3. The absence of a reflection signature in

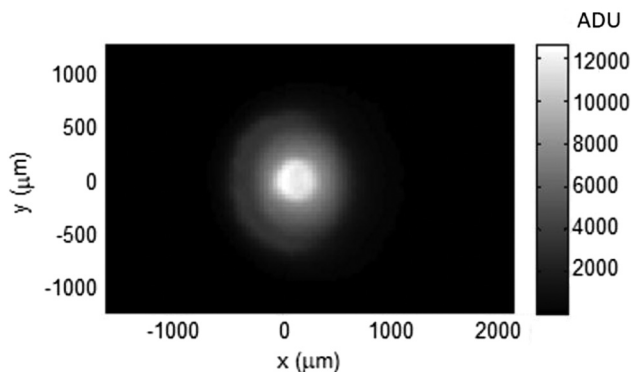


FIG. 3. SWIR thermogram of the melt pool during a low power laser melting experiment. The front of the melt pool is located to the left.

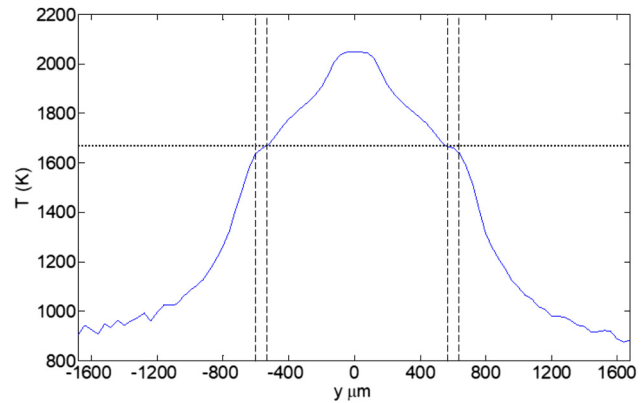


FIG. 4. SWIR lateral temperature estimation across the melt pool for low power laser melting. The dashed vertical lines indicate the edges of the melt pool and the mushy region.

the VNIR temperature profile suggests that the hyperspectral camera was directed slightly more toward the front of the melt pool. The available temperatures around the reflection suggest a peak temperature inside the melt pool of around 1950 K, corresponding with the hyperspectral calculations which indicate a temperature between 1950 and 2100 K. The SWIR thermogram also reveals a relatively uniform signature distribution inside the melt pool, implying no strong spatial emissivity variations in the SWIR region, similar to the VNIR emissivity distribution calculated from the hyperspectral measurements.⁷

The hyperspectral temperature estimations are only valid within the fully liquid region due to large fitting errors in the mushy region and a low VNIR energy content in the lower temperatures outside the melt pool (beyond $600\ \mu\text{m}$). Being more sensitive to larger

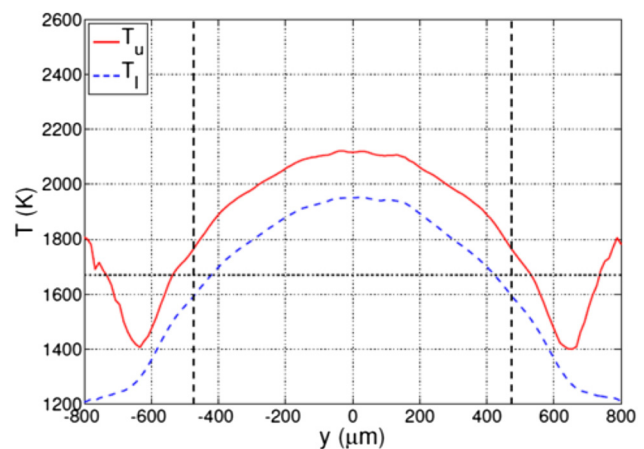


FIG. 5. Lateral temperature estimation across the melt pool during low power laser melting based on VNIR hyperspectral data (Ref. 13). T_u and T_l indicate the upper and lower temperature limits, respectively.

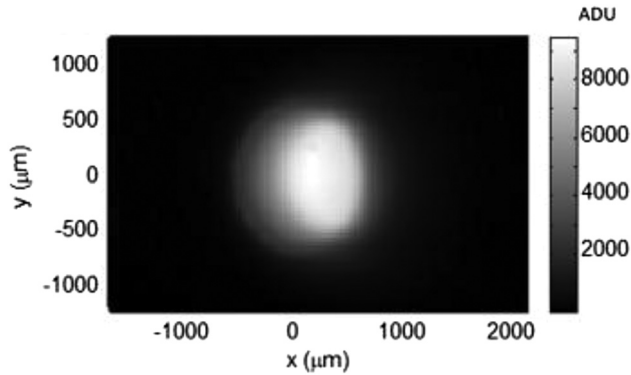


FIG. 6. SWIR thermogram of the melt pool during a high power laser melting experiment. The front of the melt pool is located to the left.

wavelengths, the SWIR measurements reveal that once outside the mushy region, the temperature follows an exponential decline toward room temperature. The SWIR camera registers a temperature of approximately 1000 K at $y = 1100 \mu\text{m}$, after which the ADU levels become too low to provide reliable signal-to-noise values.

Figure 6 shows the SWIR thermogram of the melt pool during laser melting at 500 W, and Fig. 7 contains the corresponding temperature curve calculated from the SWIR measurements. It should be recalled that the exposure time of the SWIR camera was cut down by half during the high power experiments, hence the lower ADU values. In this case, the lateral temperature profile was not extracted from the center of the thermogram, but at a location shifted $400 \mu\text{m}$ toward the front of the melt pool. It is clear from the SWIR recordings that a large nozzle reflection zone has formed from the center to the tail (0 – $600 \mu\text{m}$) of the melt pool, obscuring the useful thermal signatures. The SWIR temperature curve indicates a peak temperature of 2000 K, which is 100 K higher than the

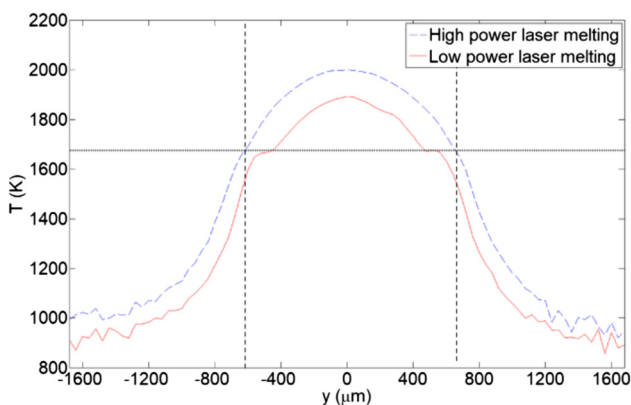


FIG. 7. SWIR lateral temperature estimation across the melt pool for high and low power laser melting, extracted at $x = -400 \mu\text{m}$. The dashed vertical lines indicate the edges of the melt pool.

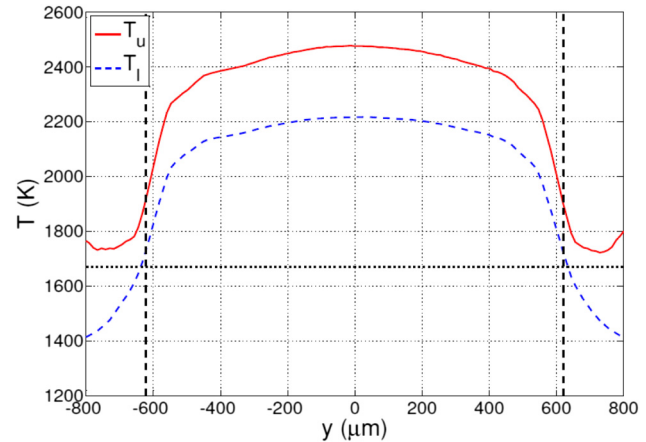


FIG. 8. Lateral temperature estimation across the melt pool during high power laser melting based on VNIR hyperspectral data (Ref. 13). T_u and T_l indicate the upper and lower temperature limits, respectively.

peak temperature measured at low laser power at the same position, and melt pool boundaries at -600 and $640 \mu\text{m}$. The melt pool edge is less pronounced than in the case of low power melting, both for the SWIR and hyperspectral VNIR measurements, indicating a smaller mushy zone due to the elevated temperatures. Outside the melt pool, the temperature decay is measured down to approximately 1100 K at $y = 1100 \mu\text{m}$.

The flat shape of the corresponding temperature curves obtained from the hyperspectral data, which are displayed in Fig. 8, may suggest that the line camera was directed toward the reflection zone during the measurements. This would explain the unusual steep temperature decline near the melt pool edges and could lead to a possible overestimation of the melt pool temperatures. A possible indication for the validity of these estimations is the value of the fitting error of the calculated temperatures, which reflects the deviation of the measured spectrum from the black body behavior. These values were indeed found to be elevated, but for the moment, no further conclusions can be drawn as to the exact error on the temperature measurements. The melt pool width is in good correspondence with the SWIR measurements, around $1240 \mu\text{m}$.

B. Laser cladding

The previous experiments were repeated, but with the addition of a powder flow which creates a clad in the wake of the melt pool and effectively recreates the monitoring conditions expected during additive manufacturing by laser metal deposition. Due to the more dynamic nature of the process, the following SWIR results are time averaged over only 20 frames, or 0.02 s.

Figure 9 shows the SWIR thermogram of the melt pool during laser cladding at 350 W, with the corresponding lateral temperature profiles presented in Figs. 10 and 11. The clad formed by the incoming powder particles can be seen on the positive x axis of the SWIR thermogram. Note how the melt pool temperatures are lower than was the case during laser melting, presumably due to

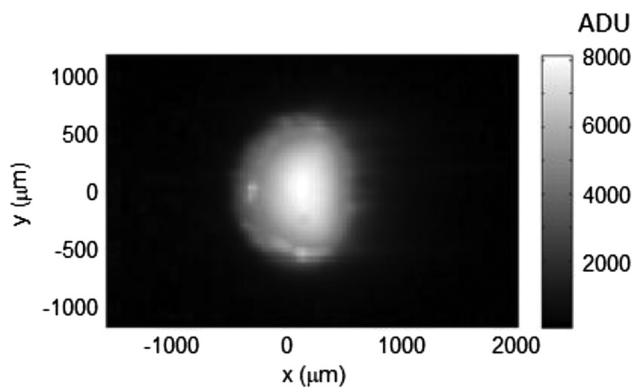


FIG. 9. SWIR thermogram of the melt pool during a low power laser cladding experiment. The front of the melt pool is located to the left.

enhanced fluid mixture at powder impact. The peak temperature derived from the SWIR measurements is just below 1900 K, again showing similarities with the lower temperature limit obtained from the hyperspectral data. The measurements indicate a temperature of 1100 K at $y = 1100 \mu\text{m}$.

Unlike the results obtained during low power laser melting, the shape of the temperature curve is insufficient to get a clear localization of the melt pool boundaries. Hot particles in and around the mushy zone result in misleading gradient changes in the temperature profile, as is the case around $-500 \mu\text{m}$ in Fig. 10. The actual edge of the melt pool is located a little bit further, around $-600 \mu\text{m}$, as indicated by the melting point and the opposing melt pool boundary at $640 \mu\text{m}$. Similar small disturbances can be noted in the temperature curves obtained from the hyperspectral measurements. These disturbances, along with the fluctuating nature of the melt pool, make the interpretation of thermal measurements during laser cladding less straightforward than during

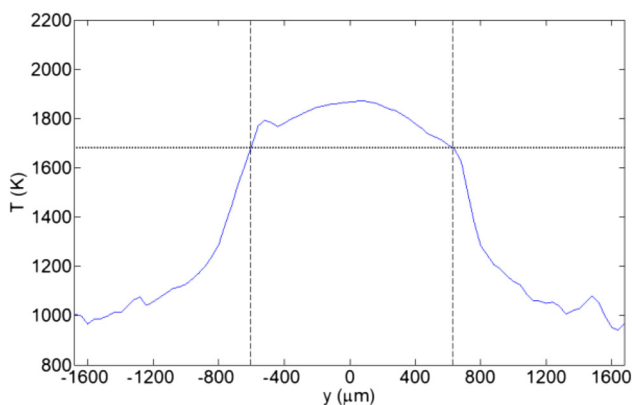


FIG. 10. SWIR lateral temperature estimation across the melt pool for low power laser cladding. The dashed vertical lines indicate the edges of the melt pool.

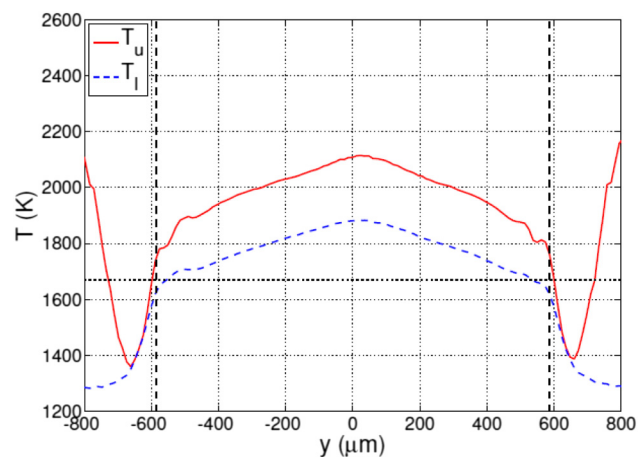


FIG. 11. Lateral temperature estimation across the melt pool during low power laser cladding based on VNIR hyperspectral data (Ref. 13). T_u and T_l indicate the upper and lower temperature limits, respectively.

laser melting and makes it more difficult to discern details near the edge of the melt pool. The mushy region, which is only a few pixels wide, is not clearly defined as was the case during laser melting. The emissivity estimation plots obtained from the hyperspectral measurements can provide an additional, more robust indication of the melt pool edge. Inside the mushy region, the spectral emissivity shows a nonlinear dependency on the wavelength, which causes apparent emissivity peaks between 500 and $600 \mu\text{m}$ in Fig. 12. The larger peaks, which are located just outside the melt pool boundary, can be attributed to regions of oxidation. It should be noted that the emissivity values presented in this paper are only valid within

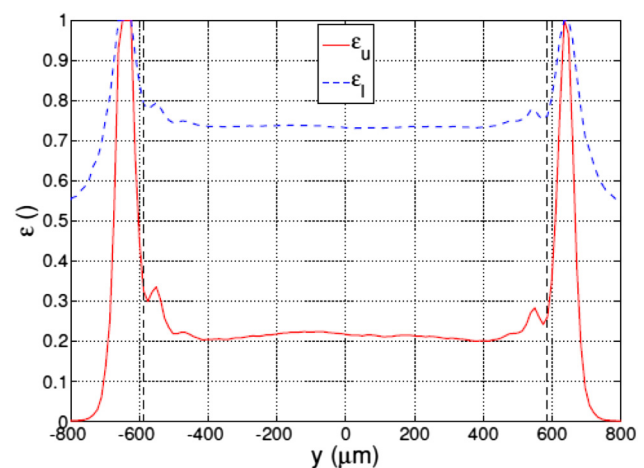


FIG. 12. Lateral emissivity estimation across the melt pool during high power laser cladding based on VNIR hyperspectral data (Ref. 13). ϵ_u and ϵ_l indicate the upper and lower emissivity limits, respectively.

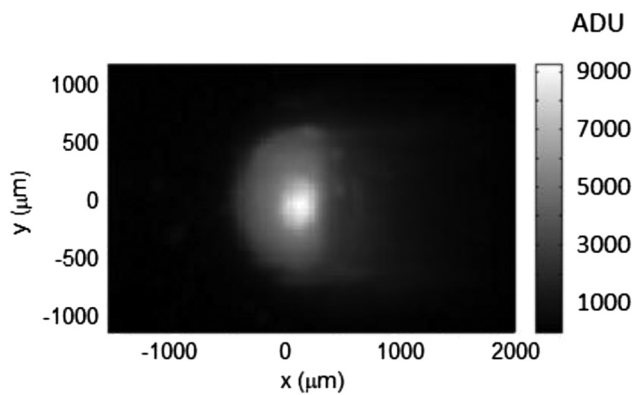


FIG. 13. SWIR thermogram of the melt pool during a high power laser cladding experiment. The front of the melt pool is located to the left.

the VNIR spectrum and that these values have been measured at an inclination of 38° relative to the surface normal.

Figures 13–16 show the measurements obtained during high power laser cladding. Based on the available temperature values around the nozzle reflection, which causes an apparent temperature rise between -200 and $200\ \mu\text{m}$ in both the SWIR and VNIR hyperspectral measurements, the melt pool peak temperature is $1950\ \text{K}$ or higher.

It should be noted that, for all the performed experiments, there seems to be a large similarity between the temperature estimations based on the SWIR measurements and the lower temperature limit derived from the hyperspectral VNIR data. The assumption of dealing with a gray body and a spatially independent emissivity in the SWIR spectrum, on the one hand, and a linearly decreasing spectral emissivity with an offset of 1 for VNIR measurements, on the other hand, seem to lead to agreeing results on the temperature

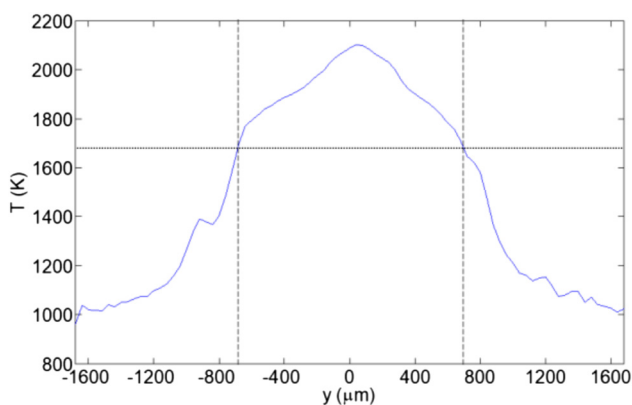


FIG. 14. SWIR lateral temperature estimation across the melt pool for high power laser cladding. The dashed vertical lines indicate the edges of the melt pool.

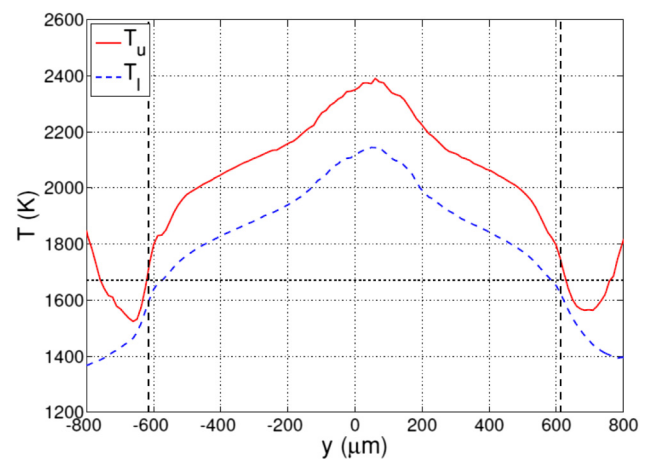


FIG. 15. Lateral temperature estimation across the melt pool during high power laser cladding based on VNIR hyperspectral data (Ref. 13). T_u and T_l indicate the upper and lower temperature limits, respectively.

distribution inside the stainless steel melt pool and even in its immediate surroundings. Still, it is known that the spectral emissivity of metals in the SWIR spectrum typically shows a small negative slope with increasing wavelength, albeit not as strong as is the case in the VNIR range. The calculated SWIR temperatures are therefore expected to underestimate the actual melt pool temperature, and it is assumed that, should a temperature estimation algorithm be used taking into account a spectral emissivity which decreases linearly with wavelength, the resulting SWIR temperature profiles would be raised somewhere between the upper and lower temperature limits calculated from the hyperspectral data.

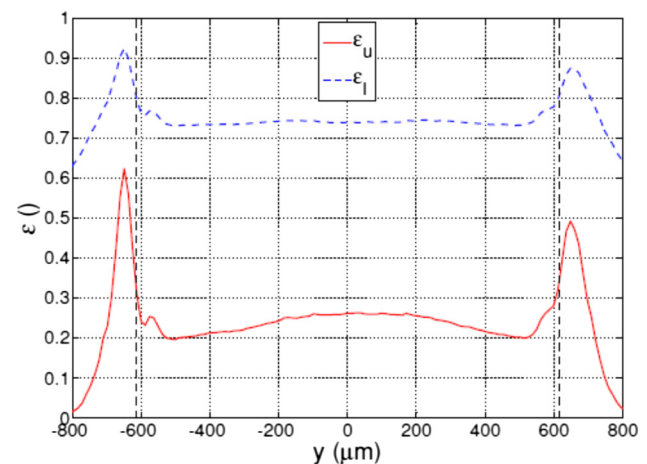


FIG. 16. Lateral emissivity estimation across the melt pool during high power laser cladding based on VNIR hyperspectral data (Ref. 13). ϵ_u and ϵ_l indicate the upper and lower emissivity limits, respectively.

The melt pool width derived from the SWIR measurements ($1300\mu\text{m}$) is slightly larger than indicated on the hyperspectral data in Figs. 13 and 14 ($1140\mu\text{m}$). These small changes can be a result of the positioning of the hyperspectral line camera and the differences in spatial resolution between the measurement systems, as well as the previously discussed disturbance factors blurring the melt pool boundary. The temperature outside the melt pool is estimated at 1100 K around $y = 1100\mu\text{m}$.

V. CONCLUSIONS

This paper presented the comparison between two camera-based methods to estimate the temperature distribution in and around a 316L stainless steel melt pool during laser melting and cladding. The first method is based on the use of a thermal SWIR camera to convert the measured radiance into absolute temperatures by assuming a gray body and a constant emissivity for the whole region of interest. The second method uses a hyperspectral VNIR line camera to fit the measured spectrum to a black body model with a spectral emissivity which decreases linearly with the wavelength, resulting in an upper and lower limit for the temperature distribution inside the melt pool.

Both methods show agreeing results with respect to the temperature distribution inside the melt pool, with the SWIR estimations showing a tendency to mirror the lower temperature limit calculated from the hyperspectral VNIR data. The gray body simplification assumed for the SWIR measurements seems to hold but is suspected to result in a slight underestimation of the actual temperatures.

Using the SWIR camera, it was possible to estimate the temperatures of the solid region around the melt pool, up to $500\mu\text{m}$ past the melt pool boundary. The position of the melt pool edges can also be derived from both VNIR and SWIR measurements, but disturbances due to hot powder particles and melt pool fluctuations make it difficult to detect the small transition zone from liquid to solid materials. During laser cladding and high laser power melting, the position of the melt pool edge should be estimated based on the melting point, not the shape of the temperature curves.

The two-dimensional SWIR thermograms reveal an additional challenge encountered during the thermal monitoring of the laser melting and cladding processes. A nozzle reflection is visible on the melt pool surface during all laser melting and cladding experiments, which influences the thermal measurements made by both SWIR and VNIR cameras and, if not properly interpreted, leads to a local overestimation of the melt pool temperature.

Regarding the cladding processes, the main differences observed between the high and low power tests is a difference in clad width and peak temperature, both of which reach a larger value during the high power tests. A visual inspection of the clads shows that both experiments resulted in fully formed clads. Future work will include the *in situ* analysis of the melt pool geometry and absolute temperatures in and around the melt pool in order to obtain information on (subsurface) structural defects, residual stresses, and the microstructure of the clad material.

ACKNOWLEDGMENT

This work was supported by the Research Foundation—Flanders (FWO).

REFERENCES

- ¹D. L. Bourell, M. C. Leu, and D. W. Rosen, *Roadmap for Additive Manufacturing: Identifying the Future of Freeform Processing* (The University of Texas at Austin, Austin, TX, 2009).
- ²L. Song and J. Mazumder, "Feedback control of melt pool temperature during laser cladding process," *IEEE Trans. Control Syst. Technol.* **19**, 1349–1356 (2011).
- ³D. Salehi and M. Brandt, "Melt pool temperature control using Lab-VIEW in Nd:YAG laser blown powder cladding process," *Int. J. Adv. Manuf. Technol.* **29**, 273–278 (2006).
- ⁴Th. Duvaut, "Comparison between multiwavelength infrared and visible pyrometry: Applications to metals," *Infrared Phys. Technol.* **51**, 292–299 (2008).
- ⁵M. Doubenskaia, M. Pavlov, S. Grigoriev, and I. Smurov, "Definition of brightness temperature and restoration of true temperature in laser cladding using infrared camera," *Surf. Coat. Technol.* **220**, 244–247 (2013).
- ⁶W. Devesse, D. De Baere, and P. Guillaume, "High resolution temperature measurement of liquid stainless steel using hyperspectral imaging," *Sensors* **17**, 91 (2017).
- ⁷W. Devesse, D. De Baere, M. Hinderdael, and P. Guillaume, "High resolution temperature estimation during laser cladding of stainless steel," *Phys. Procedia* **83**, 1253–1260 (2016).
- ⁸M. Planck, *Vorlesungen über die Theorie der Wärmestrahlung* (J.A. Barth, Leipzig, 1913).
- ⁹J. R. Davis, *Metals Handbook Desk Edition*, 2nd ed. (ASM International, Materials Park, OH, 1998).
- ¹⁰E. Hagen and H. Rubens, "Über Beziehungen des Reflexions- und Emissionsvermögens der Metalle zu ihrem elektrischen Leitvermögen," *Ann. Phys.* **316**, 873–901 (1903).
- ¹¹W. Coblenz and R. Stair, "Reflecting power of beryllium, chromium and several other metals," *Bur. Stand. J. Res.* **2**, 343–354 (1929).
- ¹²N. Yoshiharu and T. Hideo, "Surface properties of polished stainless steel," *Ann. CIRP* **29**, 409–412 (1980).
- ¹³W. Devesse, *Development and Validation of Innovative Modeling, Monitoring and Control Strategies for 3D Metal Printing* (VUB press, Brussels, Belgium, 2017), 239 pp.

Meet the Authors

Margot Lison started pursuing a Ph.D. in 2017 at the Acoustic and Vibrations Research Group of the Vrije Universiteit Brussel after receiving an M.Sc. degree in aeronautical engineering. Having successfully completed a Master thesis involving the development of a robotic NDT system based on line scan thermography for the evaluation of full-scale aircraft parts, she decided to make the jump to a new field of study: additive manufacturing. She is now active in developing nondestructive in-process monitoring strategies for metal additive manufacturing, currently focusing on implementing thermography NDT into the manufacturing process to improve the quality of AM produced parts.

Wim Devesse received an M.Sc. degree in mechanical engineering from KTH Royal Institute of Technology, Stockholm, Sweden, in 2012 and an M.Sc. degree in electro-mechanical engineering from the Vrije Universiteit Brussel, Brussels, Belgium, in 2013. He received his Ph.D. degree in 2017 at the Vrije Universiteit Brussel. He received the IEEE-CASE Best Student Paper Award in 2013. He is a student member of IEEE and LIA.

Dieter de Baere received a Master degree in industrial sciences and technology in electro-mechanical engineering at the Katholieke Hogeschool Brugge-Oostende, Ostend, Belgium, in 2004. He received an M.Sc. degree of electro-mechanical engineering in aeronautics from the Vrije Universiteit Brussel, Brussels, Belgium in 2006. From

2006 to 2012, he worked as a Test & Development Engineer for Asco Industries. In 2012, he joined Vrije Universiteit Brussel as a Ph.D. student.

Michaël Hinderdael received an M.Sc. degree in mechanical engineering from the Vrije Universiteit Brussel and the Université Libre de Bruxelles, Brussels, Belgium, in 2014. He received a Ph.D. degree in 2018 at the Department of Mechanical Engineering of the Vrije Universiteit Brussel, where he is currently doing

postdoctoral research on structural health monitoring solutions for additive manufactured components.

Patrick Guillaume received an M.Sc. degree in mechanical-electrotechnical engineering in 1987 from the Vrije Universiteit Brussel, Brussels, Belgium. In 1987, he joined the Department of Electrical Engineering at the Vrije Universiteit Brussel and received a Ph.D. degree in 1992. He joined the Department of Mechanical Engineering in 1996 where he is currently the Chair of the department.